Engineering xxx (xxxx) xxx

Contents lists available at ScienceDirect

Engineering

journal homepage: www.elsevier.com/locate/eng

Article

An Ultracompact Spoof Surface Plasmon Sensing System for Adaptive and Accurate Detection of Gas Using a Smartphone

Xuanru Zhang [a,b,c], Jia Wen Zhu [a,c], Tie Jun Cui [a,b,c,*]

[a] State Key Laboratory of Millimeter Waves and Institute of Electromagnetic Space, Southeast University, Nanjing 210096, China
[b] School of Information Science and Engineering, Southeast University, Nanjing 210096, China
[c] School of Microelectronics, Southeast University, Nanjing 210096, China

ARTICLE INFO

Article history:
Available online xxxx

Keywords:
Spoof surface plasmons
Internet of Things
Integrated sensing
Resonance tracking
Microwave sensing

ABSTRACT

Resonantly enhanced dielectric sensing has superior sensitivity and accuracy because the signal is measured from relative resonance shifts that are immune to signal fluctuations. For applications in the Internet of Things (IoT), accurate detection of resonance frequency shifts using a compact circuit is in high demand. We proposed an ultracompact integrated sensing system that merges a spoof surface plasmon resonance sensor with signal detection, processing, and wireless communication. A software-defined scheme was developed to track the resonance shift, which minimized the hardware circuit and made the detection adaptive to the target resonance. A microwave spoof surface plasmon resonator was designed to enhance sensitivity and resonance intensity. The integrated sensing system was constructed on a printed circuit board with dimensions of 1.8 cm × 1.2 cm and connected to a smartphone wirelessly through Bluetooth, working in both frequency scanning mode and resonance tracking mode and achieving a signal-to-noise ratio of 69 dB in acetone vapor sensing. This study provides an ultracompact, accurate, adaptive, sensitive, and wireless solution for resonant sensors in the IoT.

1. Introduction

Resonantly enhanced dielectric sensing exhibits superior sensitivity and accuracy based on the signals measured from relative resonance shifts that are immune to signal fluctuations [1]. A wide variety of such resonant sensors exists; surface plasmons (SPs) [2–4] and microcavities [5–8] working in optical frequencies may be the most well-known. Radiofrequency identification (RFID) tags [9,10] and printed resonators embedded in circuits [11,12] operating at microwave frequencies fall into this category. The sensing signal originates from the permittivity change (the imaginary part of the complex impedance) of the transducer materials. It has been validated that dielectric sensing can improve the linearity, dynamic range, stability, and accuracy compared with resistive sensing, which measures the real part of the impedance change of the same transducer material [13]. Resonantly enhanced dielectric sensing has broad applications and has been used for real-time monitoring of biomedical targets [5,7,14,15], gases [13], strains [9,10], humidity [16], and temperature [17].

The flourishing Internet of Things (IoT) has increased the requirements for sensor robustness, low cost, and compactness [18]. In this context, low frequencies, such as microwaves and radio frequencies are preferred in non-laboratory field applications because optical and terahertz sensing usually require bulky instruments and an optical table. For millimeter waves, the costs are high and the debugging of active devices is complex. However, microwave sensing is limited by its low sensitivity and large resonator size, owing to its long wavelength. Thus, multiple compressions of the effective wavelength at low frequencies may be an effective strategy. Spoof SPs (SSPs) that mimic the physical properties of optical SPs based on artificial metal structures [19–26] enable deep-wavelength compression and high sensitivity, providing a promising avenue for microwave resonant sensing [11]. The SSP concept was proposed in 2004 and was experimentally realized in ultrathin metal patterns in planar circuits in 2013 [19,21], including traveling and localized modes. Localized SSPs combine standing-wave enhancement and plasmonic enhancement of sensitivity [11]. The compatibility of SSPs with printed circuit boards (PCBs) and integrated circuits (ICs) makes them integrable with subsequent analog and digital circuits, making them suitable for IoT sensors [21,24,27–32]. Additionally, the strong modal confinement of SSPs leads to low coupling with free-space

* Corresponding author at: State Key Laboratory of Millimeter Waves and Institute of Electromagnetic Space, Southeast University, Nanjing 210096, China.
E-mail address: tjcui@seu.edu.cn (T.J. Cui).

https://doi.org/10.1016/j.eng.2023.05.013

Please cite this article as: X. Zhang, J.W. Zhu and T.J. Cui, An Ultracompact Spoof Surface Plasmon Sensing System for Adaptive and Accurate Detection of Gas Using a Smartphone, Engineering, https://doi.org/10.1016/j.eng.2023.05.013

electromagnetic (EM) fields. Thus, good EM compatibility (EMC), which is critical for increasingly complicated EM environments and crowded EM spectra, is expected. As a new field, microwave SSP sensing has grown rapidly with attempts in chemical sensing [33], monitoring of engineering structures [34], and dielectric measurements [35,36].

Integrated sensors have become a popular trend in the IoT, merging sensors with signal detection, processing, and communication systems, and providing immediate accessibility to sensing data with compact equipment [9,37,38]. However, accurate detection of resonance-frequency shifts in compact circuits remains a challenge. Amplitude or intensity measurements at a single frequency have been performed using integrated resonant sensors [9,10,13], although they are susceptible to signal fluctuations. Other attempts include scanning the frequency back and forth over the resonance range to determine the dip or peak position, the same as in an on-bench measurement using vector network analyzers (VNAs). Integrated microwave resonant sensors were conceptually proposed some time ago using a microcontroller unit (MCU) to tune the frequency of a voltage-controlled oscillator (VCO) [39]. However, the scanning process is time-consuming and requires numerous spectral resources. Recently, significant efforts have been made toward resonance tracking using phase-locked loops (PLLs) [40–42]. However, the circuit must be designed elaborately from the basic transistors for each specific case; the settings are fixed during the design and lack versatility in different sensing scenarios. In addition, the circuit size is large for state-of-the-art prototypes.

In this study, we report an ultracompact and accurate integrated microwave SSP sensing system. A microwave SSP resonator (SSPR) was designed to simultaneously enhance sensitivity and resonance intensity. A software-defined resonance-tracking scheme with automatically determined control parameters was developed and executed in an MCU, which minimized the circuit volume and made the detection intelligently adaptable to the target resonance. The sensing system communicated and interacted with a smartphone via Bluetooth. The total size of the system is 1.8 cm $\times$ 1.2 cm. A signal-to-noise ratio (SNR) of 69 dB, data rate of approximately 2272 measuring points per second, and good EMC performance were achieved. The sensing function was validated using acetone vapor sensing. This study provides an ultracompact, accurate, and intelligent wireless solution for integrated resonant sensors and envisions the broad prospects of SSPRs in IoT sensors.

2. Results and discussion

2.1. System architecture

A diagram of the integrated microwave SSP sensing system is shown in Fig. 1(a). All hardware devices, including periphery circuits, were covered by a multilayer PCB with a size of 1.8 cm $\times$ 1.2 cm, except for a button cell, as shown in Figs. 1(b) and (c). The total thickness of the PCB including the device height was approximately 4.94 mm (see Section S1 in Appendix A for details). The sensing system transferred data to and received instructions from a smartphone. The sensing signal was measured using the resonance frequency of the SSPR. Similar to all resonance sensors, the function of the SSP sensing system is versatile and depends on the transducer material attached to the resonator surface (Section S2 in Appendix A). Sensing specificity originates from the specific reactions of the transducer materials with the sensing targets. In this study, the sensing function was validated by acetone vapor sensing using a polydimethylsiloxane (PDMS) film. The PDMS film swelled after absorbing acetone vapor, and its effective permittivity increased [43–48]. Thus, the resonance frequency decreased with increasing acetone vapor concentration.

The signal detection and processing circuit, which converts the resonance shift of the SSPR to a voltage signal, is a minimal circuit including a VCO, a detector diode, and an MCU, as shown in Fig. 1(d). The resonance-tracking loop was primarily realized using an algorithm in the MCU. Instructed by the smartphone, the sensing system works in both the frequency scanning mode, which sweeps over each frequency point and presents the resonance curve, and the resonance tracking mode, which locks the VCO frequency to the instant resonance frequency of the SSPR and outputs the VCO controlling voltage as the sensing signal. The working frequency of the VCO was controlled by the digital-to-analog converter (DAC) voltage from the MCU. The transmitted power of the SSPR was detected by a detector diode and sent to the analog-to-digital converter (ADC) of the MCU. In the following discussion, the horizontal and vertical coordinates of the measured SSPR transmittance spectrum represent the DAC and ADC voltages.

The working frequency of the integrated sensing system was approximately 4.9 GHz; the system can be conveniently redesigned for other frequencies based on specific EM environments or other considerations. The working frequency was close to the resonance frequency of the SSPR and could be tuned by varying the size and pattern of the SSPR. The VCO and detector were selected to cover the working band. Transducer materials usually operate in a relatively broad spectrum compared to SSPR and other devices.

2.2. Design and analysis of SSPR sensor

An SSPR in a sandwich excitation structure was designed for simultaneous enhancement of the resonance intensity and sensitivity, as shown in Figs. 2(a) and (b). A standalone SSPR metallic pattern with a thickness of 0.1 mm (made of stamped stainless steel and plated by copper, see Appendix A for details) was located above the PCB, with an intermediate PDMS film of 50 μm thickness inserted between the SSPR and PCB (see Section S1 and S3 in Appendix A for the detailed layout). The microstrip pattern printed on the PCB top layer was widened from the 50 Ω microstrip line to provide efficient excitation. The field distributions of the SSPR modes are shown in Fig. 2(c). The simulated and on-PCB-measured transmittance spectra of the proposed SSPR are presented in Fig. 2(d) (for details on the EM simulation, see Section S3). The upper and lower *x*-axes were calibrated using the frequency-tuning curve of the VCO. The SSPR resonated at approximately 4.92 GHz, indicating that the resonance was confined to a diameter of 1/14.2 wavelength. Based on the spoof plasmonic confinement of the spoke-like resonator, the resonance mode was further folded by the slit, breaking the spatial symmetry and inducing a circling current (see Section S3 for a detailed mode analysis) [26]. Deep-subwavelength confinement involves multiple effective wavelength compressions and results in high sensitivity at the same working wavelength. Intuitively, the proposed SSPR was quantitatively compared with a common microstrip ring resonator (MRR) operating in the same band (see Section S4 in Appendix A for details on the MRR). The same SSPR pattern printed on the top layer was chosen as a contrast to demonstrate the effects of the sandwich structure.

The resonance intensity δT, defined as the difference between the top and bottom of the transmittance resonance curve (Fig. 2(d)), was significantly enhanced by the sandwiching structure. The resonance intensity is a key issue in on-PCB measurements; it requires full use of the specific ADC resolution and affects the overall noise level (Section S5 in Appendix A). Feeding a deep-subwavelength resonator is challenging; capacitive coupling is commonly used to enhance resonance intensity [26,49]. However, capacitive coupling significantly decreases sensitivity because the

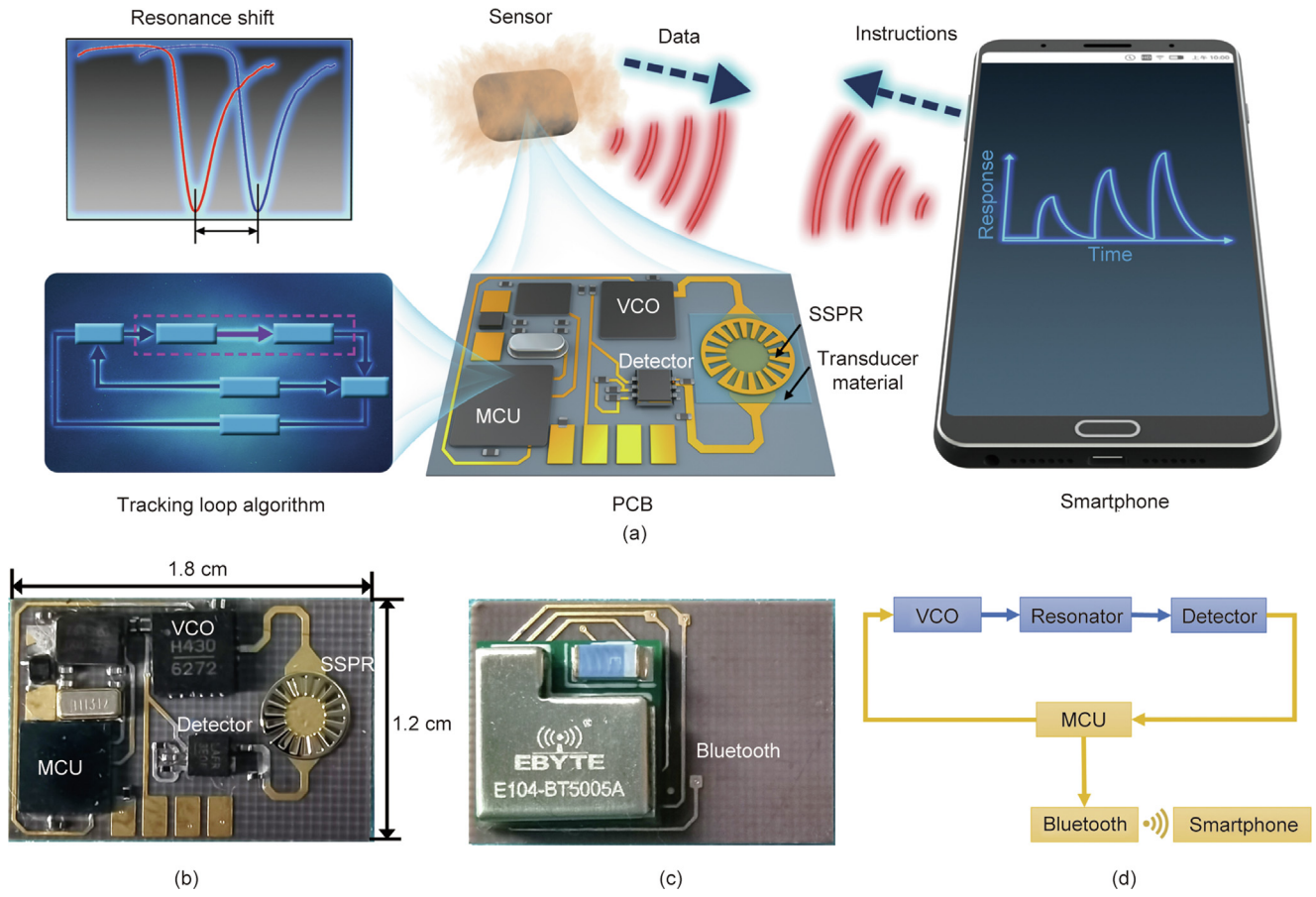

Fig. 1. Compact integrated sensing system to track resonance shift of SSPR: (a) Schematic of integrated SSP sensing system, including signal processing circuit and sensing network; (b, c) photographs of integrated sensing system: (b) top view and (c) bottom view; (d) block diagram of hardware system of integrated sensing system. The blue blocks indicate the main microwave analog circuit, and the yellow blocks indicate the digital computation and communication circuits.

EM resonance fields are partly attracted to the inert capacitance, lowering the effective interactions of the modes with the dielectric. In this study, the proposed sandwiching structure simultaneously enhanced sensitivity and resonance intensity. As shown in Fig. 2(d), the simulated δT is −5.8 dB, which is greatly enhanced from −1.1 dB when the same SSPR is printed on the PCB top layer (Section S4).

As shown in Figs. 2(e) and (f), the resonance shift sensitivity of the proposed SSPR was clearly enhanced compared with that of the contrast MRR. The enhanced sensitivity can be attributed to several factors. From the EM resonance point of view, the maximum electric field enhancement of the SSPR was 2.7 times that of the contrast MRR, assuming that the same power was fed into the resonators (as shown in Fig. 2(c) and Section S4), which theoretically indicates a larger sensitivity according to the perturbation theory of resonators [50]. This enhancement is attributed to deep-subwavelength confinement and spoof plasmonic enhancement. From a structural perspective, sandwiching the PDMS film between the SSPR and top microstrip pattern of the PCB causes the EM fields to concentrate in the PDMS film. Because the resonance fields can interact adequately with the PDMS film in the sandwiching structure, the sensitivity is further enhanced to 9.7 times that of the same SSPR geometry printed on the microstrip layer (top metal layer) with the transducer materials on the top of the resonator. The contrast mode also possesses spoof plasmonic enhancements but its EM fields are mainly concentrated inside the PCB substrate. To highlight the effect of deep-subwavelength confinement and quantize the overall enhancement, we define the local sensitivity (S_L) as

$$S_L = \left(\frac{\mathrm{d}f_r}{\mathrm{d}\varepsilon}\right) \cdot \left(\frac{1}{S}\right) \tag{1}$$

where f_r is the resonance frequency; ε is the relative permittivity of the PDMS film, and S is the resonator area. S_L evaluates the sensing response within a unit size and indicates the distinguishing capabilities of small permittivity perturbations. The details of S_L calculations can be found in Section S4. The local sensitivity of the proposed SSPR was 108 times that of the MRR resonating in the same band.

Comparing the two transmittance curves in Fig. 2(d), there is a clear degradation in the Q-factor measured on the PCB. In addition to fabrication imperfections, other factors also contributed to distortion of the on-PCB measured transmittance resonance spectra, including the broadened linewidth of the VCO, varied VCO output powers depending on the tuning voltage, nonlinearity in the VCO output frequency tunability, nonlinear response of the detector to the input power, and frequency-dependent response of the detector. For a detailed analysis, please refer to Section S6 in Appendix A. By calibrating the DAC/ADC voltages to the VCO frequency and transmittance power, the on-PCB measured Q-factor was determined to be 18.5. Although this Q-factor degrades significantly, it is sufficient based on the proposed resonance-tracking scheme. Higher Q factors resulted in negligible SNR improvements (Section S7 in Appendix A). To improve the on-PCB measured

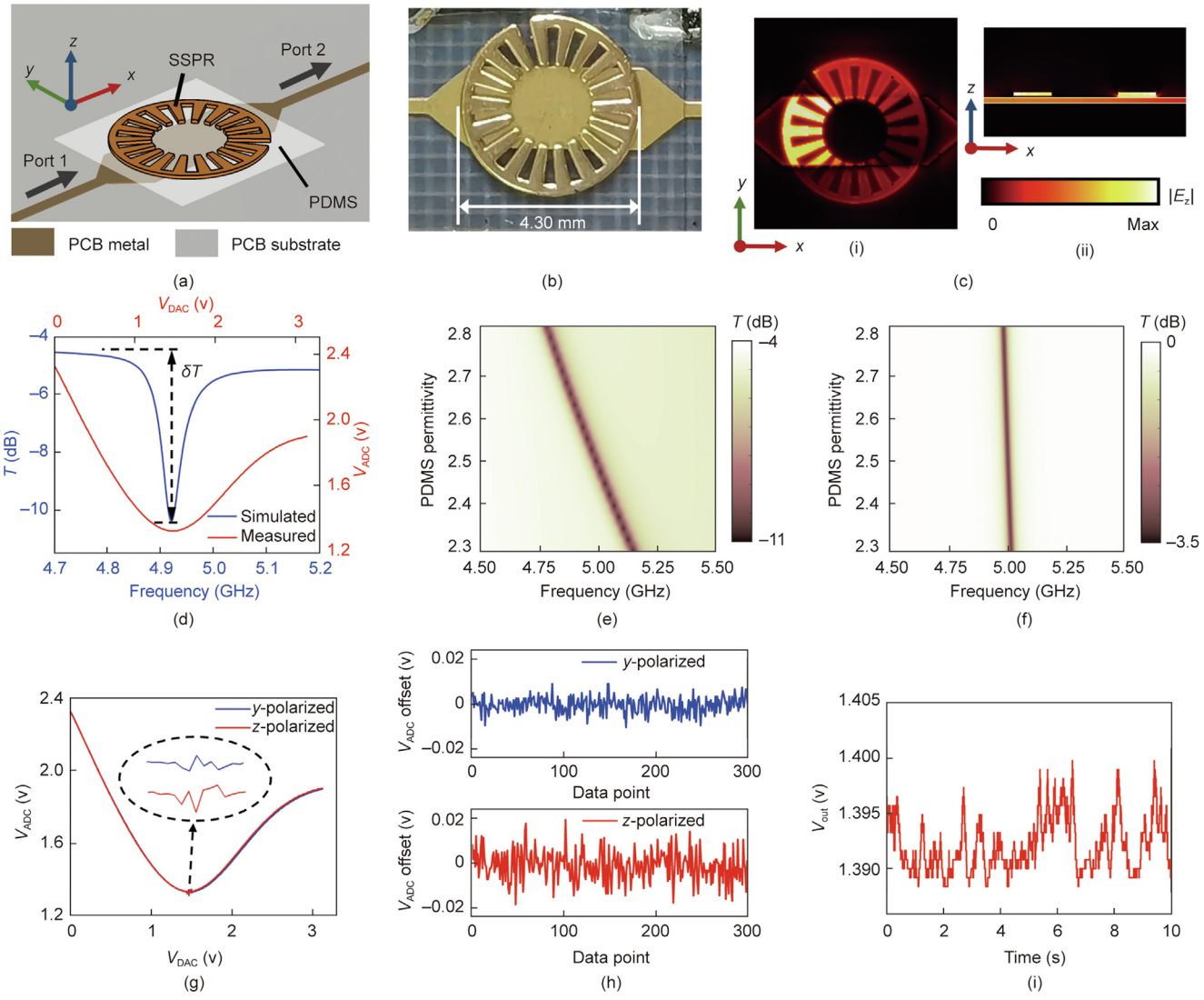

Fig. 2. Design and measurement of SSPR: (a) Design of SSPR and sandwiching excitation structure; (b) photograph of fabricated SSPR, attached to exciting microstrip pattern with interlayer of transparent PDMS film; (c) simulated $|E_z|$ distributions (i) on the resonator surface and (ii) the cross-section on *xz*-plane; (d) simulated and on-PCB measured transmittance spectra of SSPR. (e) mapping of simulated SSPR transmittance spectra varied with relative permittivity of PDMS; (f) mapping of simulated transmittance spectra for contrast MRR. (e) and (f) share the same mapping color bar; (g) measured transmittance spectra with continuous-wave (CW) interfering radiations at 4.94 GHz in *y*- and *z*-polarizations; (h) offsets of ADC voltage at bottom of resonance dip, measured with CW interfering radiations of 25 dBm at 4.94 GHz in *y*- and *z*-polarizations; (i) noise level of resonance tracking detection measured with CW interfering radiations of 25 dBm at 4.94 GHz in *z*-polarization. $|E_z|$: amplitude of the *z* component of the electric field; *T*: transmittance; δT: resonance intensity; V_{ADC}: ADC voltage; V_{DAC}: DAC voltage; V_{out}: the voltage signal output of the resonance-tracking scheme; MRR: microstrip ring resonator.

Q-factor, the SNR, VCOs, and detectors with better linearity and lower dispersion can be used. However, such devices require elaborately designed compensatory circuits. Use of filters and balancers can also improve consistency. However, the main concern is the balance between SNR and circuit size. The proposed resonance-tracking scheme can effectively suppress noise, even with such broadened peaks. Thus, no further improvements were made and the total size remained compact.

It is difficult to couple spatial waves into deep-subwavelength resonators; high immunity to EM interference (EMI) can be expected. The EMI immunity test was performed with a continuous-wave (CW) radiation of 25 dBm from horn antennas located 100 mm apart (for details, see Section S8 in Appendix A). We noticed that the strong CW radiations caused only slight interferences to the transmittance curves, even at the resonance frequency (measured as 4.94 GHz, slightly deviating from the simulated value of 4.92 GHz), as shown in Fig. 2(g). The offsets of the ADC voltage at resonance measured by fixing the VCO output frequency (the DAC voltage) and collecting the detector response (the ADC voltage (V_{ADC})) with CW-interfering radiations at 4.94 GHz are shown in Fig. 2(h). Larger offsets are generated by *z*-polarized interference because they are the main polarizations of the resonance mode and are coupled more with the SSPR. The standard deviation is 0.0067 V in Fig. 2(h) for the *z*-polarized interference, which corresponds to an SNR of 46 dB, referring to an average V_{ADC} of 1.33 V (defined as the ratio of the signal power to the noise power and presented on the dB scale in this study) [6]. In addition to frequency-scanning mode, the sensor was measured in resonance-tracking mode. The total SNR of the resonance-tracking measurement (V_{out} in Fig. 2(i) is the voltage signal output of the resonance-tracking scheme, defined and discussed in detail in the following section) degraded from 69 to 55 dB (Fig. 2(i)) with an interfering radiation of 25 dBm in the *z*-polarization at 4.94 GHz. From the emission perspective, the radiative efficiency

of the proposed SSPR was as low as −17 dB. The sensing resonator generated little radiation; the radiation to the entire sensing system originated primarily from the Bluetooth module. The SSPR and the software-defined resonance-tracking scheme contributed to good EMC performance. From a hardware point of view, the software-defined scheme minimizes the hardware circuit and allows an ultracompact PCB board (1.8 cm × 1.2 cm with an incident wavelength of 6.07 cm). The interfering power coupled from the circuit board is considerably reduced compared to that of a larger circuit board and more complex wiring. From a software perspective, the noise level in V_{out} (SNR of 55 dB) is further suppressed from that in V_{ADC} (SNR of 46 dB) owing to the real-time locking algorithm, as demonstrated in Fig. 2(h) and (i) and will be discussed in detail in the next section.

2.3. Intelligent resonance tracking scheme

We developed a Pound–Drever–Hall (PDH) locking scheme to detect the resonance shift of the SSPR using an error signal proportional to the resonance shift. It also locks the VCO output frequency at the instant resonance frequency of the SSPR. PDH locking was originally proposed for laser frequency stabilization via a feedback control loop [51,52], and has been developed for other applications owing to its outstanding accuracy and time resolution in optical microcavity sensing [6–8], interferometric gravitational-wave detectors [53], and high-fidelity quantum control [54]. However, manipulation of such a precise locking loop and determination of control parameters are often difficult [55,56]. In this study, we developed a PDH locking scheme and operated it discretely using a self-programmed MCU algorithm that minimized circuit size and achieved high accuracy. The control parameters were adaptively determined from the target resonance.

A block diagram of the proposed scheme is shown in Fig. 3(a); the conceptual basis is shown in Fig. 3(b). The output frequency of the VCO was instantly locked to the resonance frequency of the SSPR using the loop shown in Fig. 3(a); its instant control voltage was output as the resonance-tracking signal V_{out}. Thus, V_{out} was positively correlated to the resonance frequency and shifted with respect to the target signal. A square-wave modulation signal was used to tune the V_{DAC}, implemented by hopping the resonance up and down, equivalent to only two sampling points per period for a sinusoidal modulation signal. Thus, a square-wave signal leads to a higher data rate than any other modulation function using the same MCU clock configuration. The resonance-tracking effects were the same as those with sinusoidal modulation, except for the constant coefficient in the error signal formula, as presented in the mathematical derivations and Simulink simulations in Sections S9 and S10 in Appendix A. With the discrete operations in our MCU algorithm, the data rate was determined considering both the rising time of the modulation voltage and the time delay in the operation loop (Sections S11 and S12 in Appendix A). A stable data rate of 2272 measurement points per second was achieved based on an 8 MHz, 12 bit MCU and a baud rate of 921 600 bits per second (bps). The proposed resonance-tracking scheme produced output data in a few calculation steps in a short time, leading to a higher data rate than the common frequency scanning scheme based on the same time cycle, determined by the MCU oscillators and the baud rate.

The PDH locking parameters were calculated automatically according to the transmittance spectrum, which was recorded in frequency scanning mode (Fig. 3(b)). T in Fig. 3(b) represents the transmittance; T' is its derivative. Both T and T' curves shifted during the sensing process. For clarity, only one T' curve is shown in Fig. 3(b). The starting value of V_{DAC} (V_0) in Fig. 3(a) (equivalent to f_0 in Fig. 3(b)) was determined from the resonance dip. The amplitude of the modulation signal (A_m) should generally be proportional to the resonance bandwidth; otherwise, the response transmittance differential generated in one modulation process may be overwhelmed by noise. As shown in Fig. 3(b), T' was calculated from the T spectrum and A_m was determined to be 1/8 of the width between the maximum and minimum values of T'. The value of A_m was calculated at the beginning of the resonance tracking process. The coefficient of 1/8 is experiential; we tested the resonances of different Q-factors and found that a value of 1/8 produced a good SNR in most cases. Calculating from the on-PCB measured transmittance spectrum in Fig. 2(d) and calibrating the horizontal coordinate to the frequency, A_m is determined to be 6 MHz. During resonance tracking, the instant working bandwidth was 12 MHz at a working frequency of 4.9 GHz. The consumed spectrum resources were significantly suppressed compared to the frequency scanning method.

The three control parameters K_p, K_i, and K_d of the proportional–integral–derivative (PID) controller are crucial for stable operation and accurate detection of the PDH locking loop. Determination of these parameters is typically empirical and difficult, although there are tuning guides such as the Ziegler–Nichols method [57]. The PID controller produces feedback voltage to V_{DAC} based on the error signal (taken as T' in the MCU algorithm). In our discrete implementation, the integral term (K_i) evolves into a superposition of every feedback step, and K_p and K_d are set to zero. As interpreted from the modulation triangle in Fig. 3(b), the feedback signal in one step is proportional to T' and is given by

$$-\Delta f = K_i \cdot T' \tag{2}$$

where Δf is the frequency shift.

For convenience, a parameter K is defined as the reciprocal of the slope of T':

$$K = 1/T'' \tag{3}$$

where T'' is the second derivative of T.

The value of K_i was determined based on K. When $K_i = K$, the feedback is equal to the frequency shift (the shift from the green curve to the blue curve in Fig. 3(b)). Thus, the VCO frequency can be shifted to the new instantaneous resonance position in a single step by taking a linear approximation of T'. T'' was calculated using a linear least-squares regression of T' in the $[-3A_m, 3A_m]$ interval. By reducing K_i from K, the response gradually approached the target signal in several aggregations, and can be interpreted using Eq. (3). For our sensor, the data rate was sufficiently high compared to the target signal varying rate; smaller K_i values are preferred for lower noise levels because a large K_i can lead to overshoots and oscillations in the PID control. The effects of K_i on PDH resonance tracking were analyzed via Simulink simulations for cases with and without thermal noise, as shown in Sections S10 and S13 in Appendix A. The measured SNRs were 48, 53, 60, and 62 dB for $K_i = K$, $0.5K$, $0.2K$, and $0.1K$, respectively, as shown in Fig. 3(c). However, if an excessively small K_i value is used (such as $K_i = 0.001K$), the response V_{out} signal may lag the target signal. Automatic determination of the PID control parameters can potentially be applied to any resonance case using PDH locking. For example, resonance-sensing cases are based on EM resonances ranging from microwaves to optical frequencies, mechanical resonances, and acoustic resonances. Automatic determination can be extended to laser frequency stabilization and atomic force microscopy (AFM) probe tracking. The automatic determination process was designed for a single resonance peak as there was only one resonance within the VCO band in this study. For multiple-resonance cases, the PID parameters should be determined for each resonance.

The power spectrum density (PSD) describes the power distribution over frequency and is defined as the Fourier transform of

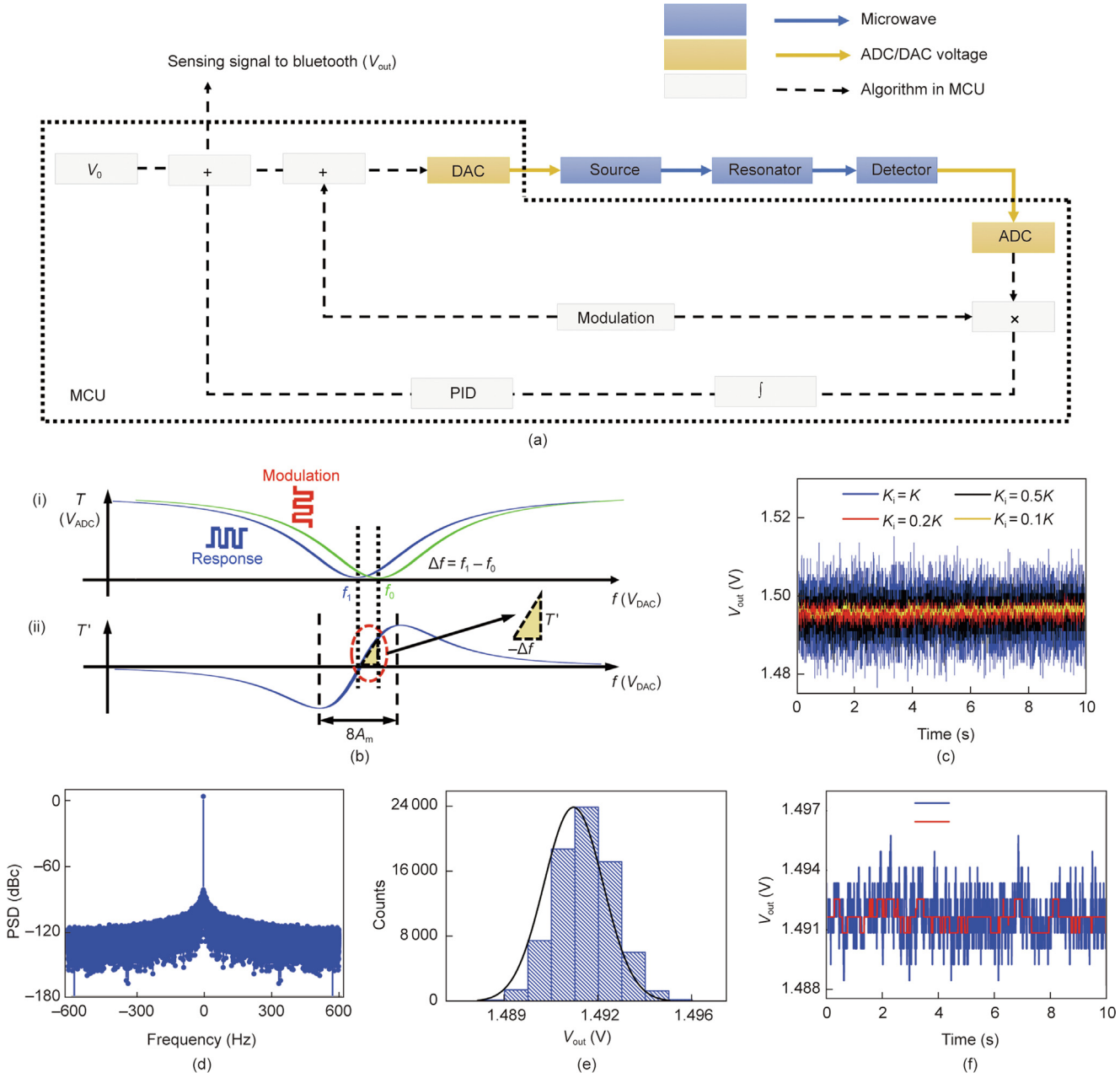

Fig. 3. Intelligent resonance tracking scheme: (a) block diagram of resonance tracking loop. The signals in the hardware circuit are denoted by solid lines, whereas the signals in the algorithm are denoted by dashed lines. Blue indicates the microwave signals; yellow indicates the ADC/DAC voltages. The blocks within the dotted black line represent the algorithm in the MCU. (b) Conceptual basis of resonance tracking scheme using a square-wave modulation signal, and automatic calculation method of A_m and K. (c) Noise level of resonance tracking detection when K_i is set as K, 0.5 K, 0.2 K, and 0.1 K. (d) Power spectrum density (PSD) of raw noise level data when K_i = 0.1 K. (e) Histogram and fitted Gaussian distribution function of raw noise level data when K_i = 0.1 K. (f) Raw and filtered noise level data when K_i is set to 0.1 K. The window size of the median filter is 300. PID: proportional–integral–derivative; V_0: starting value of V_{DAC}; T': derivative of the transmittance T; f: frequency; Δf: frequency shift; f_1: shifted resonance frequency; f_0: original resonance frequency; A_m: amplitude of the modulation signal; K: parameter defined in Eq. (3); K_i: the integral control parameter of the PID controller.

the $V_{out}(t)$ noise level [6,7]. Fig. 3(d) presents the PSD calculated from the $K_i = 0.1K$ curve in Fig. 2(c). Histograms of the $K_i = 0.1K$ signal with the fitted Gaussian distribution functions are shown in Fig. 3(e) [6,7]. The noise was Gaussian but not white as the noise level was higher at lower frequencies. The thermal noise of the hardware circuit was measured at V_{ADC} as 67 dB (see Section S13 for details). The noise characteristics were consistent with those reported for PDH locking of optical resonators [6,7]. In the software-defined PDH scheme, the noise level can be conveniently processed using a median filter. The raw and processed data using a median filter with a window size of 300 are shown in Fig. 3(f). The median filter sets each point as the average of all surrounding points within the window. The SNR was further improved from 62 to 69 dB using a median filter ($K_i = 0.1K$). Larger window sizes can further improve the SNR but may blur some detailed information. The window size should be based on the data rate and target signal trend.

2.4. System demonstration for acetone vapor sensing

As a proof-of-concept, the integrated system was validated by acetone vapor sensing using PDMS films as transducer materials. A correspondence between the acetone concentration and effective permittivity of PDMS has been reported, laying the foundation for acetone sensing [43–48]. The coordinates and units were chosen to be consistent with those shown in Fig. 3, using V_{out} directly as the

sensing signal. The operational flow of the sensing system is shown in Fig. 4(a); Video S1 in Appendix A and (ii) and (iii) of Fig. 4(a) show the screens for the frequency-scanning and resonance-tracking processes. The curves are dynamically displayed in both frequency-scanning and resonance-tracking modes. PDH locking starts with the automatically calculated A_m and K_i = K. The PID parameters can be manually set on the PID setting page, with automatically calculated values displayed on the smartphone for reference. Resonance-tracking data were processed using a median filter with a window size of 300. Using the "smooth" function, the displayed data are filtered by a median filter with a window size of 3000. The "relock" function on the resonance tracking page is designed to restart the resonance tracking process with automatically calculated control parameters. This was designed to address a common issue in PDH locking, in which locking fails when the target signal changes abruptly or the PID parameters are not suitable. The data collection methods between the integrated sensor and the smartphone or computer are described in Section S14 in Appendix A.

Fig. 4(b) shows a photograph of the sensing system operating on a smartphone. In addition to the PCB, only a button cell was required for operation. For acetone vapor sensing, a dynamic gas-mixing system was constructed to control the acetone vapor concentration, as shown in Section S15 in Appendix A. The interflow rate was fixed at 1 L·min^{-1} to reduce possible temperature jitter caused by the flow. A median filter with a window size of 3000 was used. The response voltage V_{out} of the sensing system with increasing concentrations of acetone vapor is shown in Fig. 4(c). V_{out} decreased with increasing acetone vapor concentration. Air flowed after 12 min and V_{out} increased as the PDMS film released the absorbed acetone. V_{out} changed at approximately 0.04 V when the acetone vapor concentration increased from 0 to 10 000 ppm (1 ppm = 0.386 mg·m^{-3} for acetone vapor). Assuming a linear response of V_{out} to the acetone vapor concentration and a confidence factor of 3.2 [58,59], the detection limit was calculated as follows:

$$\text{Detection limit} = 3.2 \times 5.3 \times 10^{-4}\,\text{V} \times (10000\,\text{ppm}/0.04\,\text{V}) = 425\,\text{ppm} \quad (4)$$

where the standard deviation is 5.3 × 10^{-4} V according to the SNR of 69 dB, and the baseline is approximately 1.5 V. The detection limit was only 1/58 of the lower explosive limit of acetone [60]. The responses to sequential acetone and air pulses are shown in

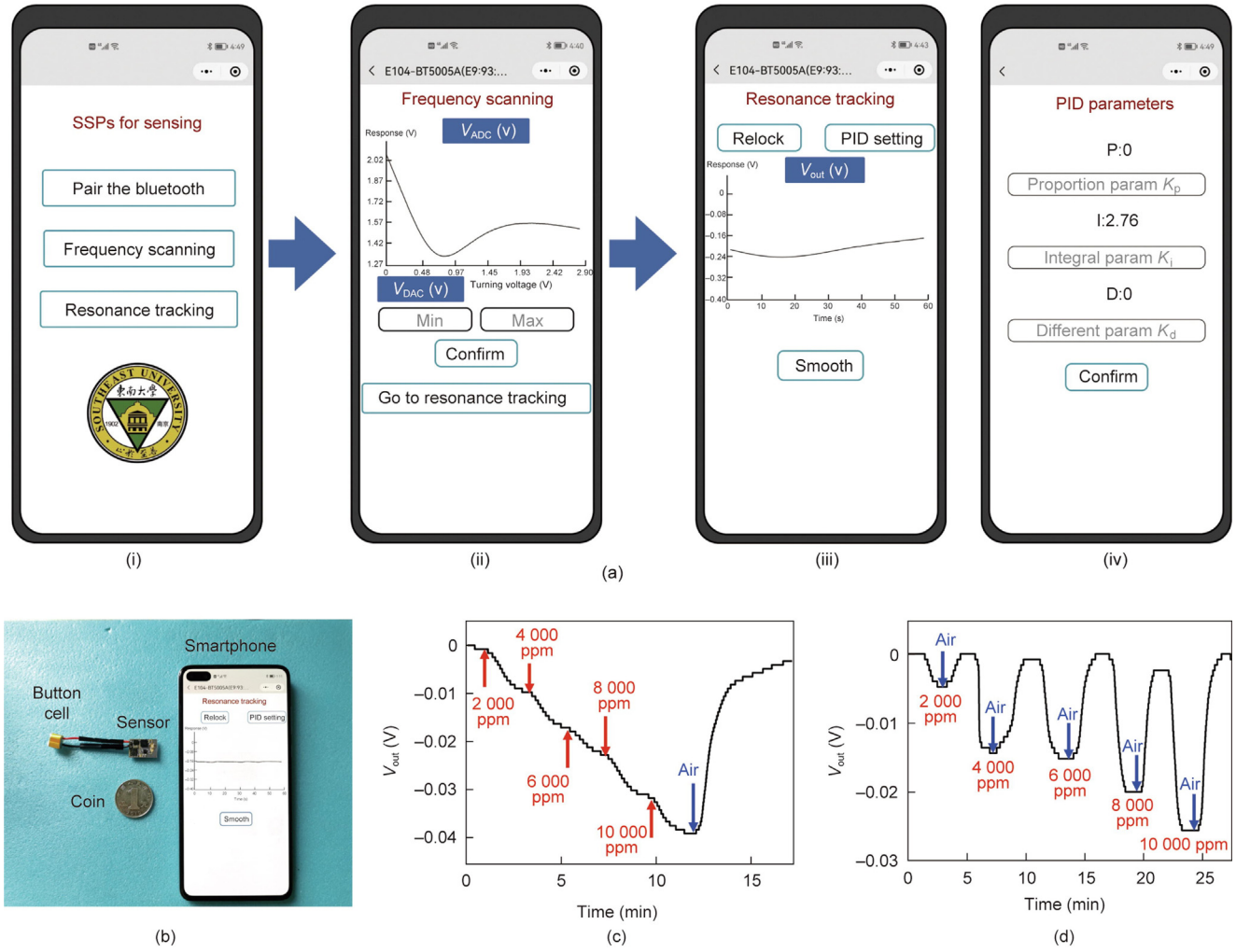

Fig. 4. Acetone vapor-sensing experiments using the integrated system: (a) Smartphone user interface for (i) function menu, (ii) frequency scanning, (iii) resonance tracking, and (iv) user-defined PID parameter setting; (b) Photograph of sensor working with smartphone; the size of the sensing system is compared with a coin with a diameter of 2.5 cm; (c) Response of sensing system to increasing concentrations of acetone vapor; (d) Response of sensing system to acetone vapor pulses with different concentrations. The concentrations in red refer to acetone vapor pulses. The "Air" texts with blue arrows refer to the moment when air pulses are injected. For acetone vapor concentration, 1 ppm ≈ 2.59 mg·m^{-3}.

Fig. 4(d). The responses were reproducible, and the acetone absorption was reversible. Comparing the signals at 10000 ppm in Fig. 4(c) and (d), a slight hysteresis was observed, which is common for gas sensing [61] (for details, see Section S16 in Appendix A). The qualitative monitoring of acetone evaporation is shown in Video S2 in Appendix A.

The detection limit and dynamic range depend on both the sensing system and transducer materials. This study emphasizes physical and electrical investigations that present outstanding sensitivity and SNR and envision promising detection limits. The acetone vapor detection limit can be improved by replacing PDMS with transducer materials that produce larger permittivity changes when the target gas is absorbed [55,56].

3. Conclusions

We reported an ultracompact, sensitive, accurate, and intelligent wirelessly integrated microwave SSP sensing system, and demonstrated its application in acetone vapor sensing. The proposed SSPR addresses the sensitivity and EMI issues of microwave resonant sensors. The software-defined resonance-tracking scheme minimizes the hardware circuit and consumed spectrum resources, and makes resonance-shift detection intelligently adaptive to the target resonance. It can be used for printed resonators embedded in circuits and for wirelessly excited RFID tags based on either rigid or flexible circuit boards. Broadly, ultracompact and intelligent PDH locking can be extended to mechanical and acoustic resonant sensors based on on-PCB integrated tunable sources and detectors. The ultrahigh compactness and accuracy of the proposed sensing system promote its application in smart homes and the IoT.

Acknowledgments

This work was supported by the National Natural Science Foundation of China, China (62288101, 61701108, and 61631007), the National Key Research and Development Program of China, China (2017YFA0700201, 2017YFA0700202, and 2017YFA0700203), the Major Project of Natural Science Foundation of Jiangsu Province, China (BK20212002), and the 111 Project, China (111-2-05).

Compliance with ethics guidelines

Xuanru Zhang, Jia Wen Zhu, and Tie Jun Cui declare that they have no conflict of interest or financial conflicts to disclose.

Appendix A. Supplementary data

Supplementary data to this article can be found online at https://doi.org/10.1016/j.eng.2023.05.013.

References

[1] Luttge R. Microfabrication for industrial application. Oxford: William Andrew; 2011.
[2] Maier SA. Plasmonics: fundamentals and applications. New York City: Springer; 2007.
[3] Barnes WL, Dereux A, Ebbesen TW. Surface plasmon subwavelength optics. Nature 2003;424(6950):824–30.
[4] Homola J, Piliarik M. Surface plasmon resonance (SPR) sensors. New York City: Springer; 2006.
[5] Jiang X, Qavi AJ, Huang SH, Yang L. Whispering-gallery sensors. Matter 2020;3(2):371–92.
[6] Heylman KD, Thakkar N, Horak EH, Quillin SC, Cherqui C, Knapper KA, et al. Optical microresonators as single-particle absorption spectrometers. Nat Photonics 2016;10(12):788–95.
[7] Su J, Goldberg AFG, Stoltz BM. Label-free detection of single nanoparticles and biological molecules using microtoroid optical resonators. Light Sci Appl 2016;5:e16001.
[8] Zhi Y, Yu XC, Gong Q, Yang L, Xiao YF. Single nanoparticle detection using optical microcavities. Adv Mater 2017;29(12):1604920.
[9] Niu S, Matsuhisa N, Beker L, Li J, Wang S, Wang J, et al. A wireless body area sensor network based on stretchable passive tags. Nat Electron 2019;2(8):361–8.
[10] Dautta M, Alshetaiwi M, Escobar A, Torres F, Bernardo N, Tseng P. Multifunctional hydrogel-interlayer RF/NFC resonators as a versatile platform for passive and wireless biosensing. Adv Electron Mater 2020;6(4):1901311.
[11] Zhang X, Cui WY, Lei Y, Zheng X, Zhang J, Cui TJ. Spoof localized surface plasmons for sensing applications. Adv Mater Technol 2021;6(4):2000863.
[12] Chen LY, Tee BCK, Chortos AL, Schwartz G, Tse V, Lipomi DJ, et al. Continuous wireless pressure monitoring and mapping with ultra-small passive sensors for health monitoring and critical care. Nat Commun 2014;5:5028.
[13] Potyrailo RA, Go S, Sexton D, Li X, Alkadi N, Kolmakov A, et al. Extraordinary performance of semiconducting metal oxide gas sensors using dielectric excitation. Nat Electron 2020;3(5):280–9.
[14] Allison G, Sana AK, Ogawa Y, Kato H, Ueno K, Misawa H, et al. A Fabry-Pérot cavity coupled surface plasmon photodiode for electrical biomolecular sensing. Nat Commun 2021;12:6483.
[15] Minopoli A, Della Ventura B, Lenyk B, Gentile F, Tanner JA, Offenhäusser A, et al. Ultrasensitive antibody-aptamer plasmonic biosensor for malaria biomarker detection in whole blood. Nat Commun 2020;11:6134.
[16] Najeeb MA, Ahmad Z, Shakoor RA. Organic thin-film capacitive and resistive humidity sensors: a focus review. Adv Mater Interfaces 2018;5(21):1800969.
[17] Liao J, Yang L. Optical whispering-gallery mode barcodes for high-precision and wide-range temperature measurements. Light Sci Appl 2021;10:32.
[18] Čolaković A, Hadžialić M. Internet of Things (IoT): a review of enabling technologies, challenges, and open research issues. Comput Netw 2018;144:17–39.
[19] Pendry JB, Martín-Moreno L, Garcia-Vidal FJ. Mimicking surface plasmons with structured surfaces. Science 2004;305(5685):847–8.
[20] Hibbins AP, Evans BR, Sambles JR. Experimental verification of designer surface plasmons. Science 2005;308(5722):670–2.
[21] Shen X, Cui TJ, Martin-Cano D, Garcia-Vidal FJ. Conformal surface plasmons propagating on ultrathin and flexible films. Proc Natl Acad Sci USA 2013;110(1):40–5.
[22] Pors A, Moreno E, Martin-Moreno L, Pendry JB, Garcia-Vidal FJ. Localized spoof plasmons arise while texturing closed surfaces. Phys Rev Lett 2012;108(22):223905.
[23] Huidobro PA, Shen X, Cuerda J, Moreno E, Martin-Moreno L, Garcia-Vidal FJ, et al. Magnetic localized surface plasmons. Phys Rev X 2014;4(2):021003.
[24] Shen X, Cui TJ. Ultrathin plasmonic metamaterial for spoof localized surface plasmons. Laser Photonics Rev 2014;8(1):137–45.
[25] Williams CR, Andrews SR, Maier SA, Fernández-Domínguez AI, Martín-Moreno L, García-Vidal FJ. Highly confined guiding of terahertz surface plasmon polaritons on structured metal surfaces. Nat Photonics 2008;2(3):175–9.
[26] Zhang X, Cui TJ. Deep-subwavelength and high-Q trapped mode induced by symmetry-broken in toroidal plasmonic resonator. IEEE Trans Antennas Propag 2021;69(4):2122–9.
[27] Tian X, Lee PM, Tan YJ, Wu TLY, Yao H, Zhang M, et al. Wireless body sensor networks based on metamaterial textiles. Nat Electron 2019;2(6):243–51.
[28] Li Z, Tian X, Qiu C, Ho JS. Metasurfaces for bioelectronics and healthcare. Nat Electron 2021;4(6):382–91.
[29] Liu Y, Xu KD, Li J, Guo YJ, Zhang A, Chen Q. Millimeter-wave E-plane waveguide bandpass filters based on spoof surface plasmon polaritons. IEEE Trans Microw Theory Tech 2022;70(10):4399–409.
[30] Zhang X, Tang WX, Zhang HC, Xu J, Bai GD, Liu JF, et al. A spoof surface plasmon transmission line loaded with varactors and short-circuit stubs and its application in Wilkinson power dividers. Adv Mater Technol 2018;3(6):1800046.
[31] Guo YJ, Xu KD, Deng X, Cheng X, Chen Q. Millimeter-wave on-chip bandpass filter based on spoof surface plasmon polaritons. IEEE Electron Device Lett 2020;41(8):1165–8.
[32] Liang Y, Yu H, Feng G, Apriyana AAA, Fu X, Cui TJ. An energy-efficient and low-crosstalk sub-THz I/O by surface plasmonic polariton interconnect in CMOS. IEEE Trans Microw Theory Tech 2017;65(8):2762–74.
[33] Zhou YJ, Li QY, Zhao HZ, Cui TJ. Gain-assisted active spoof plasmonic Fano resonance for high-resolution sensing of glucose aqueous solutions. Adv Mater Technol 2020;5(1):1900767.
[34] Annamdas VGM, Soh CK. Contactless load monitoring in near-field with surface localized spoof plasmons—a new breed of metamaterials for health of engineering structures. Sens Actuator A 2016;244:156–65.
[35] Guo YJ, Xu KD, Deng X. Tunable enhanced sensing of ferrite film using meander-shaped spoof surface plasmon polariton waveguide. Appl Phys Express 2019;12(11):115502.
[36] Li X, Liu L, Zhou Z, Shen J, Zhang Y, Han G, et al. Highly sensitive and topologically robust multimode sensing on spoof plasmonic skyrmions. Adv Opt Mater 2022;10(15):2200331.
[37] Gao W, Emaminejad S, Nyein HYY, Challa S, Chen K, Peck A, et al. Fully integrated wearable sensor arrays for multiplexed *in situ* perspiration analysis. Nature 2016;529(7587):509–14.
[38] Kwon K, Kim JU, Deng Y, Krishnan SR, Choi J, Jang H, et al. An on-skin platform for wireless monitoring of flow rate, cumulative loss and temperature of sweat in real time. Nat Electron 2021;4(4):302–12.

[39] Fratticcioli E, Dionigi M, Sorrentino R. A simple and low-cost measurement system for the complex permittivity characterization of materials. IEEE Trans Instrum Meas 2004;53(4):1071–7.
[40] Elhadidy O, Shakib S, Krenek K, Palermo S, Entesari K. A wide-band fully-integrated CMOS ring-oscillator PLL-based complex dielectric spectroscopy system. IEEE Trans Circuits Syst I 2015;62(8):1940–9.
[41] Elhadidy O, Elkholy M, Helmy AA, Palermo S, Entesari K. A CMOS fractional-*N* PLL-based microwave chemical sensor with 1.5% permittivity accuracy. IEEE Trans Microw Theory Tech 2013;61(9):3402–16.
[42] Helmy AA, Jeon HJ, Lo YC, Larsson AJ, Kulkarni R, Kim J, et al. A self-sustained CMOS microwave chemical sensor using a frequency synthesizer. IEEE J Solid-State Circuits 2012;47(10):2467–83.
[43] St-Gelais R, Mackey G, Saunders J, Zhou J, Leblanc-Hotte A, Poulin A, et al. Gas sensing using polymer-functionalized deformable Fabry-Pérot interferometers. Sens Actuator B 2013;182:45–52.
[44] Mohammadi S, Zarifi MH. Differential microwave resonator sensor for real-time monitoring of volatile organic compounds. IEEE Sens J 2020;21(5):6105–14.
[45] Zarifi MH, Sohrabi A, Shaibani PM, Daneshmand M, Thundat T. Detection of volatile organic compounds using microwave sensors. IEEE Sens J 2015;15(1):248–54.
[46] Rumens CV, Ziai MA, Belsey KE, Batchelor JC, Holder SJ. Swelling of PDMS networks in solvent vapours; applications for passive RFID wireless sensors. J Mater Chem C 2015;3(39):10091–8.
[47] Rydosz A, Maciak E, Wincza K, Gruszczynski S. Microwave-based sensors with phthalocyanine films for acetone, ethanol and methanol detection. Sens Actuator B 2016;237:876–86.
[48] Ge W, Jiao S, Chang Z, He X, Li Y. Ultrafast response and high selectivity toward acetone vapor using hierarchical structured TiO_2 nanosheets. ACS Appl Mater Interfaces 2020;12(11):13200–7.
[49] Sun S, Zhu L. Wideband microstrip ring resonator bandpass filters under multiple resonances. IEEE Trans Microw Theory Tech 2007;55(10):2176–82.
[50] Waldron RA. Perturbation theory of resonant cavities. Proc IEE Part C 1960;107(12):272–4.
[51] Drever RWP, Hall JL, Kowalski FV, Hough J, Ford GM, Munley AJ, et al. Laser phase and frequency stabilization using an optical resonator. Appl Phys B 1983;31:97–105.
[52] Black ED. An introduction to Pound–Drever–Hall laser frequency stabilization. Am J Phys 2001;69(1):79–87.
[53] Abbott BP, Abbott R, Adhikari R, Ajith P, Allen B, Allen G, et al. LIGO: the laser interferometer gravitational-wave observatory. Rep Prog Phys 2009;72(7):076901.
[54] Levine H, Keesling A, Omran A, Bernien H, Schwartz S, Zibrov AS, et al. High-fidelity control and entanglement of Rydberg-atom qubits. Phys Rev Lett 2018;121(12):123603.
[55] Li QX, Zhang X, Zhu LX, Yan SH, Jia AA, Luo YK, et al. Intelligent and automatic laser frequency locking system using pattern recognition technology. Opt Lasers Eng 2020;126:105881.
[56] Guo X, Zhang L, Liu J, Chen L, Fan L, Xu G, et al. An automatic frequency stabilized laser with hertz-level linewidth. Opt Laser Technol 2022;145:107498.
[57] Ziegler JG, Nichols NB. Optimum settings for automatic controllers. Trans ASME 1942;64(8):759–65.
[58] Mocak J, Bond AM, Mitchell S, Scollary G. A statistical overview of standard (IUPAC and ACS) and new procedures for determining the limits of detection and quantification: application to voltammetric and stripping techniques (technical report). Pure Appl Chem 1997;69(2):297–328.
[59] Quesada-González D, Stefani C, González I, de la Escosura-Muñiz A, Domingo N, Mutjé P, et al. Signal enhancement on gold nanoparticle-based lateral flow tests using cellulose nanofibers. Biosens Bioelectron 2019;141:111407.
[60] Bailly G, Harrabi A, Rossignol J, Stuerga D, Pribetich P. Microwave gas sensing with a microstrip interDigital capacitor: detection of NH_3 with TiO_2 nanoparticles. Sens Actuator B 2016;236:554–64.
[61] Lienerth P, Fall S, Lévêque P, Soysal U, Heiser T. Improving the selectivity to polar vapors of OFET-based sensors by using the transfer characteristics hysteresis response. Sens Actuator B 2016;225:90–5.